

Optical polarizers based on graphene oxide integrated with waveguides and ring resonators

David Moss (✉ dross@swin.edu.au)

Swinburne University of Technology <https://orcid.org/0000-0001-5195-1744>

Research Article

Keywords: nonlinear optics, integrated photonics, silicon, graphene oxide, Kerr nonlinearity

Posted Date: September 9th, 2021

DOI: <https://doi.org/10.21203/rs.3.rs-885241/v1>

License:  This work is licensed under a Creative Commons Attribution 4.0 International License.

[Read Full License](#)

Abstract

Integrated waveguide polarizers and polarization-selective micro-ring resonators (MRRs) incorporated with graphene oxide (GO) films are experimentally demonstrated. CMOS-compatible doped silica waveguides and MRRs with both uniformly coated and patterned GO films are fabricated based on a large-area, transfer-free, layer-by-layer GO coating method that yields precise control of the film thickness. Photolithography and lift-off processes are used to achieve photolithographic patterning of GO films with precise control of the placement and coating length. Detailed measurements are performed to characterize the performance of the devices versus GO film thickness and coating length as a function of polarization, wavelength and power. A high polarization dependent loss of ~ 53.8 dB is achieved for the waveguide coated with 2-mm-long patterned GO films. It is found that intrinsic film material loss anisotropy dominates the performance for less than 20 layers whereas polarization dependent mode overlap dominates for thicker layers. For the MRRs, the GO coating length is reduced to $50\ \mu\text{m}$, yielding a ~ 8.3 -dB polarization extinction ratio between TE and TM resonances. These results offer interesting physical insights and trends of the layered GO films and demonstrate the effectiveness of introducing GO films into photonic integrated devices to realize high-performance polarization selective components.

1. Introduction

Polarization control is one of the fundamental requirements in many optical technologies [1–3]. Polarization selective devices, such as polarizers and polarization selective resonant cavities (e.g., gratings and ring resonators), are core components for polarization control in optical systems and find wide applications in polarization-division-multiplexing [4, 5], coherent optical detection [6, 7], photography [8, 9], liquid crystal display [10, 11], and optical sensing [12, 13].

To implement polarization-selective devices, a number of schemes have been proposed and demonstrated, including those based on refractive prisms [14, 15], birefringent crystals [16, 17], fiber components [18–20], and integrated waveguides [21–25]. Among them, integrated polarization-selective devices based on complementary metal-oxide-semiconductor (CMOS) compatible integrated platforms [26] offer advantages of compact footprint, high stability, mass producibility, and high scalability as functional building blocks for photonic integrated circuits (PICs) [2]. Optical waveguides with metal cladding have been widely used to implement waveguide polarizers [27, 28]. Although high polarization-dependent loss (PDL) has been achieved for these polarizers, it usually comes at the expense of high overall propagation loss and requires complicated buffer layers to achieve broadband operation. Recently, the huge optical anisotropy and broadband response of two-dimensional (2D) materials such as graphene and transition metal dichalcogenides have been widely recognized and exploited to implement polarization-selective devices [29–34], including an in-line fiber polarizer with graphene [29], graphene-polymer waveguide polarizers [30, 35], and chalcogenide glass-on-graphene waveguide polarizers [33]. However, none of these demonstrations were based on CMOS compatible platforms. Generally, the integration of 2D materials on CMOS compatible platforms requires layer transfer processes [33, 36], where exfoliated or chemical vapour deposition grown 2D membranes are attached onto dielectric

substrates (e.g., silicon and silica wafers). Despite its widespread implementation, the transfer approach itself is complex, which makes it difficult to achieve precise patterning, as well as flexible placement and large-area continuous coating on integrated devices. Accurate control of the layer position, thickness and size is critical for optimizing parameters such as mode overlap and loss for performance. Current methods significantly limit the scale of fabrication for integrated devices incorporating 2D materials.

Owing to its ease of preparation as well as the tunability of its material properties, graphene oxide (GO) has become a highly promising member of the 2D family [37, 38]. Recently [39], a broadband GO-polymer waveguide polarizer with a high PDL of ~ 40 dB was demonstrated, where the GO films were introduced onto an SU8 polymer waveguide using drop-casting methods. The GO film thickness for each drop-casting step was ~ 0.5 μm and the drop coating diameter was ~ 1.3 mm, neither being ideal for achieving precise control of the placement, thickness, and length of the GO films.

Recently [40, 41], we reported large-area, transfer-free, and high-quality GO film coating on integrated waveguides using a solution-based method with layer-by-layer deposition of GO films. Here, we use these techniques to demonstrate GO-coated integrated waveguide polarizers and polarization-selective micro-ring resonators (MRRs) on a CMOS compatible doped silica platform. We achieve highly precise control of the placement, thickness, and length of the GO films coated on integrated photonic devices by using our layer-by-layer GO coating method followed by photolithography and lift-off processes. The latter overcomes the layer transfer fabrication limitations of 2D materials and represent a significant advance towards manufacturing integrated photonic devices incorporated with 2D materials. We measure the performance of the waveguide polarizer for different GO film thicknesses and lengths versus polarization, wavelength, and power, achieving a very high PDL of ~ 53.8 dB. For GO-coated integrated MRRs, we achieve an 8.3-dB polarization extinction ratio between the TE and TM resonances, with the extracted propagation loss showing good agreement with the waveguide results. Furthermore, we present layer-by-layer characterization of the linear optical properties of 2D layered GO films, including detailed measurements that conclusively determine the material loss anisotropy of the GO films as well as the relative contribution of film loss anisotropy versus polarization-dependent mode overlap, to the device performance. These results offer interesting physical insights and trends of the layered GO films from monolayer to quasi bulk like behavior and confirm the high-performance of integrated polarization selective devices incorporated with GO films.

2. Go-coated Waveguide Polarizer

2.1 Device Fabrication

Figure 1(a) shows a schematic of a uniformly GO-coated waveguide polarizer. The waveguides were fabricated from high-index doped silica glass core surrounded by silica via CMOS compatible processes [26, 42] with chemical mechanical polishing (CMP) used as the last step to remove the upper cladding, so as to enable GO film coating on the top surface of the waveguide. GO coating was achieved with a solution-based method that yielded layer-by-layer GO film deposition, as reported previously [40, 41]. Four

steps for in-situ assembly of monolayer GO films were repeated to construct multilayer GO films on the desired substrate, with the process being highly scalable.

We uniformly coated waveguides with 1 to 10 layers of GO. Figure 1**(b)** shows the measured Raman spectra of the waveguides without GO and with 2 layers of GO, confirming the integration of GO onto the top surface by the presence of the D (1345 cm^{-1}) and G (1590 cm^{-1}) peaks of GO. The microscope images of the integrated waveguide with zero and 2 layers of GO are shown in the insets, which illustrate the good morphology of the GO films. Figure 1**(c)** shows the thickness of GO films versus the layer number characterized by atomic force microscopy. The insets show images of 1 and 10 layers of GO coated on a $2.2\text{ cm} \times 2.2\text{ cm}$ silica substrate with high uniformity. The dependence of GO film thickness versus layer number shows a nearly linear relationship, with a thickness of $\sim 2.18\text{ nm}$ on average for each layer.

In addition to the uniformly coated devices, we selectively patterned areas of GO films using lithography and lift-off processes. Apart from allowing precise control of the size and placement of the GO films, this enabled us to test the performance of the GO-coated waveguide polarizers with shorter GO coating lengths but higher film thicknesses (up to 100 layers). The chip was first spin-coated with photoresist and then patterned using photolithography to open a window on the waveguide. Next, GO films were coated on the chip using the method mentioned above and patterned via a lift-off process.

As compared with the drop-casting method that has a GO film thickness of $\sim 0.5\text{ }\mu\text{m}$ and a minimum size of about 1.3 mm for each step [39], the combination of our GO coating method with photolithography and lift-off allows precise control of the film placement, size, and thickness (with an ultrahigh resolution of $\sim 2.18\text{ nm}$), all of which are critical for optimizing the device performance including the polarization figure of merit (FOM) and four-wave mixing conversion efficiency. Further, our solution based GO coating approach, unlike for example, the sophisticated transfer processes employed for coating 2D materials such as graphene [29, 43], is capable of covering large areas (e.g., a 4 inch wafer) on dielectric substrates (e.g., silicon and silica wafers) with relatively few defects. The combination of patterning and deposition control of GO films along with large area coating capability is critical for large-scale integrated devices incorporated with GO.

2.2 Polarization Loss Measurements

We used an 8-channel single-mode fiber (SMF) array to butt couple both TE and TM polarized continuous-wave (CW) light from a tunable laser near 1550 nm into the waveguides. The mode coupling loss between the SMF array and the waveguides was $\sim 8\text{ dB/facet}$, which can readily be reduced to $\sim 1.0\text{ dB/facet}$ with mode convertors [26]. The propagation loss of the uncoated 1.5-cm-long waveguides was very low ($< 0.25\text{ dB/cm}$) and so the total insertion loss (TE = -16.2 dB ; TM = -16.5 dB) of the uncoated devices was dominated by mode coupling loss. The slight PDL of the uncoated waveguides resulted mainly from a slightly different mode-coupling mismatch but possibly also polarization dependent scattering loss from the roughness of the polished top surface.

To characterize the performance of the devices, we introduce two figures of merit (FOMs) – one for the excess propagation loss (FOM_{EPL}) and one for the overall polarization dependent loss (FOM_{PDL}):

$$FOM_{EPL} = (EPL_{TE} - EPL_{TM}) / EPL_{TM}, \quad (1)$$

$$FOM_{PDL} = PDL / EIL, \quad (2)$$

where the excess propagation losses, EPL_{TE} (dB/cm) and EPL_{TM} (dB/cm), are GO-induced excess propagation losses for the TE and TM polarizations, respectively. PDL (dB) is the polarization dependent loss defined as the ratio of the maximum to minimum insertion losses. The excess insertion loss, EIL (dB), is the insertion loss induced by the GO film over the uncoated waveguide. The EIL only considers the insertion loss induced by GO, while excluding from the overall insertion loss both the mode coupling loss between the SMF array and the waveguide as well as the propagation loss of the uncoated waveguide. In our case, since the TM polarization had the lowest insertion loss, EIL is the excess GO-induced insertion loss for the TM polarization and is given by $EIL = EPL_{TM} \cdot L$, where L is the GO coating length. Note that FOM_{EPL} only considers the propagation loss difference induced by the GO films, and so is more accurate for the characterization of their material anisotropy, whereas FOM_{PDL} is more widely used for evaluating the device performance [33] since it also includes the background (uncoated) PDL. FOM_{EPL} equals FOM_{PDL} only when the TE and TM polarized insertion losses of the uncoated waveguide are the same.

Figure 2 shows the polarization dependent (TE (in-plane) and TM (out-of-plane)) performance for both the 1.5-cm-long uniformly coated waveguides (0–10 layers), left side (i), and the patterned 2-mm-long devices (10–100 layers), right side (ii). Figure 2(a) shows the polarization dependent insertion loss. The data points depict the average values obtained from the experimental results of 3 duplicate devices and the error bars illustrate the variations for different samples. Figure 2(b) presents the PDL and EIL calculated based on the average insertion loss in Fig. 2(a). Figures 2(c) and (d) show the FOMs calculated based on Fig. 2(b) and the polar diagrams for the insertion loss, respectively.

The TE insertion loss increases much more strongly than TM with layer number, thus yielding a large PDL with low EIL and forming the basis for our high-performance polarization dependent devices. Since GO is a dielectric film, our TM-pass GO-coated waveguide polarizer is quite different from TE-pass metal-clad waveguide polarizers based on a deeper power penetration of the evanescent TM field into a lossy metal cladding [27, 28]. The PDL reached a maximum of ~ 37.4 dB for a 10 layer uniformly coated device and ~ 53.8 dB for a 100 layer patterned device, with a modest maximum EIL of ~ 5.0 dB and ~ 7.5 dB for the two devices, respectively. By optimizing the waveguide geometry to achieve a better mode overlap with the GO films [33], the EIL can be further reduced. Moreover, the PDL was still increasing at a rate of 2–3 dB/cm/layer at 100 layers, and so substantially higher PDL can be obtained using layers thicker than 200 nm. Both FOM_{EPL} and FOM_{PDL} increase with a maximum of FOM_{EPL} and FOM_{PDL} of ~ 8.2 and ~ 8.1 , respectively, at about 50 layers with the difference between them subsequently decreasing. This is because the impact of the background PDL (~ 0.3 dB) becomes smaller as the EIL increases for increased GO layer numbers.

2.3 GO Film Properties

Figure 3(a) shows the experimental propagation loss (dB/cm) extracted from Fig. 2(a) for both polarizations of the two devices, along with the TE propagation loss calculated (by means of the Lumerical FDTD commercial mode solving software) using ellipsometry measurements (at 1550 nm) for the refractive index n and extinction coefficient k of two samples having 2 layers (Fig. 3(a-i)) and 20 layers (Fig. 3(a-ii)) of GO. Since the out-of-plane (TM polarized) response of the layered GO films is much weaker [44, 45], we could only measure, via ellipsometry, the in-plane (TE polarized) n and k of the GO films (uncertainty < 3%), which were used (in conjunction with the mode solving software) to calculate the waveguide loss for the TE polarization. The simulations assume constant n , k for different GO layer numbers in each plot. In Fig. 3(a), the experimental TE propagation loss agrees extremely well with simulations for 2 and 20 layers of GO. For other thicknesses the experimental TE loss increased more rapidly with GO layer number, indicating that the intrinsic GO film loss increases with thickness. This is not surprising, and could be due to any number of effects such as increased scattering loss and absorption induced by imperfect contact between the multiple GO layers as well as interactions between the GO layers.

Figure 3. (a) Experimental waveguide propagation loss (extracted from Fig. 2(a)) for (i) a uniformly coated device with 0 – 10 layers of GO and (ii) a patterned device with 10 – 100 layers of GO. Simulated TE loss estimated by using in-plane (TE polarized) n and k for (i) 2 and (ii) 20 layers of GO obtained from ellipsometry measurements in conjunction with mode solving software (assuming constant n , k for different layer numbers in each plot). (b) Experimental loss per layer given by the experimental loss in (a) divided by the number of layers for both polarizations. (c) Material loss of the GO films for TE (k_{TE}) and TM (k_{TM}) polarizations as well as their ratio (k_{TE} / k_{TM}). The two yellow data points (labelled as “SE”) show the in-plane k measured by spectral ellipsometry (SE) for 2 and 20 layers of GO. (d) Fractional contribution to PDL from mode overlap (η_{MO}) and material loss anisotropy (η_{MA}). In (b) – (d), the solid data points refer to the results for a uniformly coated device, whereas the hollow points are for a patterned device.

Figure 3(c) shows the GO film loss (k) extracted from the waveguide loss measurements. We neglect the effect of any variations in GO film refractive index (n) on the mode overlap. The much larger film loss k for TE polarization (k_{TE}) is a reflection of the high intrinsic loss anisotropy of the GO films, which has been previously noted in a qualitative manner [46]. The results presented here are the first quantitative measurement of intrinsic film loss anisotropy in GO films, showing that the in-plane (TE) electric field loss is significantly higher than the out-of-plane (TM) loss. This material anisotropy significantly improves the polarization dependent loss of our devices, which otherwise would derive solely from the polarization dependent mode overlap with the GO films. Both k_{TE} and k_{TM} increase with layer number, with the ratio k_{TE} / k_{TM} reaching a maximum of about 5 at 4 – 10 layers after which it decreases to ~ 3 for very thick films (100 layers). This could arise from a reduction in, for example, anisotropic film stress related effects for very thick films (> 200 nm). The two k data points (marked in yellow) in Fig. 3(c) are obtained from

ellipsometry measurements, with $k_{\text{ellips}}^{2\text{-layers}} = 0.0050$ and $k_{\text{ellips}}^{20\text{-layers}} = 0.01165$, thus agreeing extremely well with the waveguide propagation loss results – $k_{\text{wg}}^{2\text{-layers}} = 0.0054$ and $k_{\text{wg}}^{20\text{-layers}} = 0.01212$. Note also that the k 's for the patterned and uniformly coated waveguides agree well for the same number (10) of GO layers.

Figure 3(d) shows the fractional contribution to the PDL from the polarization dependent mode overlap (η_{MO}) and the material film loss anisotropy (η_{MA}), where $\eta_{\text{MO}} + \eta_{\text{MA}} = 1$. We calculated η_{MO} and η_{MA} by comparing the measured propagation loss in Fig. 3(a) for both polarizations, to the propagation loss calculated assuming isotropic film properties (using the extracted k_{TE} in Fig. 3(c) for both TE and TM polarizations). For low GO layer numbers (< 10) the PDL is dominated by the material anisotropy η_{MA} at 75%, despite the overall TE loss only being 1 dB/cm/layer (at 1 – 2 layers). The contribution of the GO material anisotropy steadily decreases, becoming comparable to the mode overlap contribution, η_{MO} , at ~ 20 layers, beyond which, for very thick films (100 layers), is smaller than η_{MO} , which is about 65%. This could reflect the transition of the film properties slightly towards a bulk (isotropic) material for very thick films. However, it is also interesting to note that even for very thick films the intrinsic film loss anisotropy is still large enough to form the basis for polarization dependent devices. To reconfigure the polarization selection, it would be relatively easy to change the mode overlap, while changing the material loss anisotropy is more challenging. A possible method to implement a TE-pass GO waveguide polarizer would be to conformally coat a high-aspect-ratio waveguide with GO films on the sidewalls. Finally, we note that although our GO-coated waveguide polarizers were based on a CMOS compatible doped silica platform, these GO films can readily be introduced into other integrated platforms (e.g., silicon and silicon nitride) [47–49], offering polarization selective devices with reduced footprint.

2.4 Optical Bandwidth and Power Dependence

Figures 4(a-i) and (a-ii) illustrate the PDL of both uniformly coated and patterned waveguides versus wavelength from 1500 to 1600 nm, showing a variation less than 2 dB and confirming the broadband operation of the polarizers. Table I compares the performance of a range of silicon photonic polarizers and 2D material based optical polarizers. The bandwidth of the material anisotropy of GO thin films is very broad [37] – several hundred nanometers, even extending to visible wavelengths (Fig. 4(a-i) insets). This is a distinct advantage of GO-coated waveguide polarizers that is extremely challenging to achieve with silicon photonic polarizers [3, 21, 24]. Moreover, GO based polarizers have simpler designs with higher fabrication tolerance as compared with silicon photonic polarizers. Indeed, the latter require precise design and control of the dimensions [2, 3]. It is also interesting to note that the PDL slightly increases at longer wavelengths for both the uniformly coated and patterned devices. This is probably a result of the excitation of high-order modes in the doped silica waveguides at shorter wavelengths, which reduces the strength of the interaction between the GO films and the evanescent field leaking from the waveguides, thus leading to a degradation in PDL.

The insertion loss versus CW power is shown in Figs. 4(b-i) and (b-ii), for both samples and polarizations, indicating only a slight increase in loss for the thicker layers and only for the TE polarization, possibly due

to photo-thermal reduction of the GO film at higher powers [50]. This might also result from self-heating and thermal dissipation in the multilayer GO film, being the subject of on-going research. In contrast, since the TM polarized absorption was very low, it did not show any significant variation with power. The increase in loss for TE polarized light was reversible – indicating that the optically induced changes were reversible. Note that this slight reversible increase in loss for the TE polarization with power actually enhances the device performance. Finally, we have shown previously [38, 51] that the material properties of GO can also be permanently changed by laser-induced photo-reduction but at significantly higher power levels than those used here, with femtosecond laser pulses. This is different from the reversible photo-thermal reduction observed here.

Table I.

Performance comparison of silicon photonic polarizers and 2D material based polarizers. PDL: polarization dependent loss. IL: insertion loss. FOM: figure of merit. ER: extinction ratio. N/A: not applicable.

Device	Length [mm]	PDL [dB]	IL ^{a)} [dB]	FOM =PDL/IL	Bandwidth [nm] (≥ 20 dB ER)
Shallowly etched silicon waveguide [21]	1	25	3	8.3	> 100
Silicon subwavelength grating waveguide [24]	0.009	27	0.5	54	~ 60
Silicon nanoplasmonic slot waveguide [22]	0.001	16	2.2	7.3	ER < 20
Graphene-coated side polished fiber [29]	2.1	27	5	5.4	~ 1000
Graphene-coated polymer waveguide [30]	7	19	26	0.73	N/A ^{b)}
Chalcogenide glass-on-graphene waveguide [33]	0.4	23	0.8	29	~ 450
MoS ₂ -coated Nd:YAG waveguide [52]	10	3	0.4	7.5	ER < 20
GO-coated polymer waveguide [39]	1.3	40	6.5	6.1	> 490
GO-coated doped silica waveguide (this work)	2	54	7.5	7.2	> 540 ^{c)}
a) The ILs exclude the fiber-to-chip coupling losses.					
b) The device was only characterized at a single wavelength.					
c) We cannot precisely characterize the bandwidth due to the lack of suitable lasers. In our measurements, we achieve high PDLs of over 52.4 dB from 1500 to 1600 nm (with a variation less than 2 dB) and also a PDL of ~ 25.2 dB at 1064 nm.					

3. Polarization-selective Microring Resonators

We coated GO films onto integrated MRRs to implement polarization-selective MRRs, for applications such as polarization-handling devices in coherent receivers [53]. Figure 5(a) shows a schematic of the GO-coated polarization selective MRR, with the insets showing schematic atomic structure of GO and scanning electron microscope (SEM) image of the GO film with up to 5 layers of GO. The unclad MRR made from high-index doped silica glass was fabricated via the same CMOS compatible processes as for the integrated waveguides in **Sect. 2** [26, 54]. These devices have been extremely successful at RF and microwave applications as well as nonlinear optics and quantum optics [55–120]. The ring and the bus waveguide had the same waveguide geometry as in **Sect. 2**. The radius of the MRR was $\sim 592 \mu\text{m}$, corresponding to a free spectral range of $\sim 0.4 \text{ nm}$ ($\sim 50 \text{ GHz}$). The gap between the ring and the bus waveguide was $\sim 0.8 \mu\text{m}$. We used the same method to couple CW light to the MRR. We fabricated and tested two types of GO-coated MRR polarizers, uniformly coated with 1 – 5 layers of GO and patterned ($50 \mu\text{m}$ in length) with 10 – 100 layers of GO using the same photolithography and lift-off processes as for the patterned waveguide in **Sect. 2**. Gold markers, prepared by metal lift-off after photolithography and electron beam evaporation, were used for precise alignment and accurate placement of GO on the MRR (deviation $< 20 \text{ nm}$). Microscope images of the integrated MRR uniformly coated with 5 layers of GO and patterned with 50 layers of GO are presented in Figs. 5(b) and (c), respectively. Note that although a number of concentric rings are shown, only the center ring was coupled with the through/drop bus waveguides to form a MRR – the rest were simply used to enable easy identification by eye. There are several factors that can limit the minimum pattern length, such as the thickness of the GO film, lithography resolution, size of the GO flakes, and thickness of the photoresist. By using oxidation and vigorous ultrasonics [41], we achieved ultrasmall GO flake sizes down to $\sim 50 \text{ nm}$. For thin GO films (< 10 layers), the pattern length was mainly limited by the lithography resolution and GO flake size, whereas for thick GO films (> 50 layers), the thickness itself becomes the dominant factor. By using e-beam lithography to write patterns on a 300-nm-thick photoresist, we achieved short pattern lengths of $\sim 150 \text{ nm}$ and $\sim 500 \text{ nm}$ for 2 layers and 30 layers of GO, respectively. This confirms the high quality and resolution of the GO deposition and patterning process as well as the good adhesion between the GO film and the integrated devices.

The measured TE and TM polarized transmission spectra of the uniformly GO-coated MRR are shown in Figs. 6(a) and (b), respectively, while the transmission spectra of the patterned MRR are shown in Figs. 7(a) and (b), all measured with the same doped silica MRR at a CW power of $\sim 0 \text{ dBm}$. The resulting Q factors and extinction ratios are shown in Fig. 8(a). The uncoated MRR had high extinction ratios ($> 15 \text{ dB}$) and relatively high Q factors (180,000) (although significantly less than for buried waveguides [42]) for both polarizations. Those values decreased with GO layer number – particularly for the TE polarization, as expected. For the patterned MRR with 50 layers of GO, a maximum polarization extinction ratio (defined as the difference between the extinction ratios of the TE and TM polarized resonances) of $\sim 8.3 \text{ dB}$ was achieved. This can be further improved by optimizing the waveguide geometry, GO film thickness, and coating length to properly balance the mode overlap and material anisotropy. The propagation loss of the GO hybrid integrated waveguides for TE and TM polarizations was obtained

using the scattering matrix method to fit the measured spectra in Figs. 6 and 7 and is shown for uniformly coated (0 – 5 layers) and patterned rings (0 – 100 layers) in Figs. 8**(b-i)** and **(b-ii)**, respectively, along with the waveguide propagation loss obtained from the waveguide experiment (i.e., the experimental propagation loss in Fig. 3**(a)**). Since different resonances did not show a significant variation over small wavelength ranges, we only fit one resonance around 1549.5 nm in each measured spectrum. The fit coupling coefficients between the ring and the bus waveguide for TE and TM polarizations are ~ 0.241 and ~ 0.230 , respectively. The close agreement reflects the stability and reproducibility of our layer-by-layer GO film coating method. We also note that the propagation loss obtained from the ring resonator experiment is slightly higher than that obtained from the waveguide experiment, especially for the TE polarization. This probably results from photo-thermal reduction of GO in the resonant cavity at higher intensity. Combined with the capability of GO to enhance the nonlinear optical performance of photonic chips, [121–131] 2D GO films represent an extremely attractive material platform for linear and nonlinear integrated photonic circuits.

4. Conclusion

We demonstrate waveguide polarizers and polarization-selective MRRs incorporated with layered GO films. We achieve precise control of the placement, thickness, and length of the GO films using layer-by-layer coating of GO films followed by photolithography and lift-off. We achieve a high PDL of ~ 53.8 dB for the patterned GO-coated waveguide, and for the GO-coated integrated MRR an ~ 8.3 -dB polarization extinction ratio between the TE and TM resonances. We find that the PDL is dominated by material loss anisotropy of the GO film for thin films, and by polarization dependent mode overlap for thick films. These integrated GO hybrid waveguide polarizers and polarization-selective MRRs offer a powerful new way to implement high-performance polarization selective devices for large-scale PICs.

Declarations

Competing interests:

The authors declare no competing interests.

References

1. Y. Yan, G. Xie, M. P. Lavery, H. Huang, N. Ahmed, C. Bao, Y. Ren, Y. Cao, L. Li, Z. Zhao, A. F. Molisch, M. Tur, M. J. Padgett, A. E. Willner, *Nat. Commun.* 2014, 5, 4876.
2. D. X. Dai, J. Bauters, J. E. Bowers, *Light Sci. Appl.* 2012, 1.
3. D. X. Dai, L. Liu, S. M. Gao, D. X. Xu, S. L. He, *Laser Photonics Rev.* 2013, 7, 303.
4. S. L. Jansen, I. Morita, T. C. W. Schenk, H. Tanaka, *J. Opt. Netw.* 2008, 7, 173.
5. A. H. Gnauck, P. J. Winzer, S. Chandrasekhar, X. Liu, B. Zhu, D. W. Peckham, *J. Lightwave Technol.* 2011, 29, 373.

6. S. J. Savory, *IEEE J. Sel. Top. Quantum Electron.* 2010, 16, 1164.
7. C. R. Doerr, L. M. Zhang, P. J. Winzer, *J. Lightwave Technol.* 2011, 29, 536.
8. R. R. Anderson, *Arch. Dermatol.* 1991, 127, 1000.
9. S. B. Phillips, N. Kollias, R. Gillies, J. A. Muccini, L. A. Drake, *J. Am. Acad. Dermatol.* 1997, 37, 948.
10. C. Weder, C. Sarwa, A. Montali, G. Bastiaansen, P. Smith, *Science* 1998, 279, 835.
11. S. H. Kim, J. D. Park, K. D. Lee, *Nanotechnology* 2006, 17, 4436.
12. K. Aydin, T. A. Seliga, V. Balaji, *J. Clim. Appl. Meteorol.* 1986, 25, 1475.
13. R. E. Mayagoitia, A. V. Nene, P. H. Veltink, *J. Biomech.* 2002, 35, 537.
14. K. Serkowski, D. S. Mathewson, V. L. Ford, *Astrophys. J.* 1975, 196, 261.
15. T. J. Wang, Q. Y. He, J. Y. Gao, Y. Jiang, Z. H. Kang, H. Sun, L. S. Yu, X. F. Yuan, J. Wu, *Laser Phys.* 2006, 16, 1605.
16. E. Saitoh, Y. Kawaguchi, K. Saitoh, M. Koshihara, *IEEE Photonics J.* 2013, 5.
17. R. C. Twu, C. C. Huang, W. S. Wang, *Microw. Opt. Technol. Lett.* 2006, 48, 2312.
18. J. Wang, J. Y. Yang, I. M. Fazal, N. Ahmed, Y. Yan, H. Huang, Y. Ren, Y. Yue, S. Dolinar, M. Tur, A. E. Willner, *Nat. Photonics* 2012, 6, 488.
19. [N. Bozinovic, Y. Yue, Y. X. Ren, M. Tur, P. Kristensen, H. Huang, A. E. Willner, S. Ramachandran, *Science* 2013, 340, 1545.
20. H. R. Ren, X. P. Li, Q. M. Zhang, M. Gu, *Science* 2016, 352, 805.
21. D. X. Dai, Z. Wang, N. Julian, J. E. Bowers, *Opt. Express* 2010, 18, 27404.
22. Y. Huang, S. Y. Zhu, H. J. Zhang, T. Y. Liow, G. Q. Lo, *Opt. Express* 2013, 21, 12790.
23. M. Z. Alam, J. S. Aitchison, M. Mojahedi, *Opt. Lett.* 2012, 37, 55.
24. X. W. Guan, P. X. Chen, S. T. Chen, P. P. Xu, Y. C. Shi, D. X. Dai, *Opt. Lett.* 2014, 39, 4514.
25. J. F. Bauters, M. J. R. Heck, D. Dai, J. S. Barton, D. J. Blumenthal, J. E. Bowers, *IEEE Photonics J.* 2013, 5.
26. D. J. Moss, R. Morandotti, A. L. Gaeta, M. Lipson, *Nat. Photonics* 2013, 7, 597.
27. M. J. Bloemer, J. W. Haus, *J. Lightwave Technol.* 1996, 14, 1534.
28. J. Wang, S. Schablitsky, Z. N. Yu, W. Wu, S. Y. Chou, *J. Vac. Sci. Technol. B* 1999, 17, 2957.
29. Q. Bao, H. Zhang, B. Wang, Z. Ni, C. H. Y. X. Lim, Y. Wang, D. Y. Tang, K. P. Loh, *Nature Photonics* 2011, 5, 411.
30. J. T. Kim, C. G. Choi, *Opt. Express* 2012, 20, 3556.
31. R. E. P. de Oliveira, C. J. S. de Matos, *Sci. Rep.* 2015, 5, 16949.
32. C. Pei, L. Yang, G. Wang, Y. Wang, X. Jiang, Y. Hao, Y. Li, J. Yang, *IEEE Photonics Technol. Lett.* 2015, 27, 927.
33. L. H. Lin, Y. Song, Y. Huang, D. Kita, S. Deckoff-Jones, K. Wang, L. Li, J. Li, H. Zheng, Z. Luo, H. Wang, S. Novak, A. Yadav, C. C. Huang, R. J. Shiue, D. Englund, T. Gu, D. Hewak, K. Richardson, J. Kong, J.

- Hu, *Nat. Photonics* 2017, 11, 798.
34. S. Sathiyar, H. Ahmad, W. Y. Chong, S. H. Lee, S. Sivabalan, *IEEE Photonics J.* 2015, 7.
 35. J. T. Kim, H. Choi, *Laser Photonics Rev.* 2018, 12, 1800142.
 36. Y. Yang, R. Liu, J. Wu, X. Jiang, P. Cao, X. Hu, T. Pan, C. Qiu, J. Yang, Y. Song, D. Wu, Y. Su, *Sci. Rep.* 2015, 5, 13480.
 37. K. P. Loh, Q. Bao, G. Eda, M. Chhowalla, *Nat. Chem.* 2010, 2, 1015.
 38. X. Zheng, B. Jia, X. Chen, M. Gu, *Adv. Mater.* 2014, 26, 2699.
 39. W. H. Lim, Y. K. Yap, W. Y. Chong, C. H. Pua, N. M. Huang, R. M. De La Rue, H. Ahmad, *Opt. Express* 2014, 22, 11090.
 40. Y. Yang, J. Wu, X. Xu, Y. Liang, S. T. Chu, B. E. Little, R. Morandotti, B. Jia, D. J. Moss, *APL Photonics* 2018, 3, 120803.
 41. Y. Yang, H. Lin, B. Y. Zhang, Y. Zhang, X. Zheng, A. Yu, M. Hong, B. Jia, *ACS Photonics* 2019, 6, 1033.
 42. L. Razzari, D. Duchesne, M. Ferrera, R. Morandotti, S. Chu, B. E. Little, D. J. Moss, *Nat. Photonics* 2009, 4, 41.
 43. M. Liu, X. Yin, E. Ulin-Avila, B. Geng, T. Zentgraf, L. Ju, F. Wang, X. Zhang, *Nature* 2011, 474, 64.
 44. Y. C. Chang, C. H. Liu, C. H. Liu, Z. Zhong, T. B. Norris, *App. Phys. Lett.* 2014, 104, 261909.
 45. Y. C. Chang, C. H. Liu, C. H. Liu, S. Zhang, S. R. Marder, E. E. Narimanov, Z. Zhong, T. B. Norris, *Nat. Commun.* 2016, 7, 10568.
 46. G. Eda, A. Nathan, P. Wobkenberg, F. Colleaux, K. Ghaffarzadeh, T. D. Anthopoulos, M. Chhowalla, *App. Phys. Lett.* 2013, 102, 133108.
 47. X. Yin, T. Zhang, L. Chen, X. Li, *Opt. Lett.* 2015, 40, 1733.
 48. X. Yin, X. Ke, L. Chen, T. Zhang, J. Li, Z. Zhu, X. Li, *J. Lightwave Technol.* 2016, 34, 3181.
 49. X. Hu, J. Wang, *IEEE Photonics J.* 2017, 9, 1.
 50. W. Y. Chong, W. H. Lim, Y. K. Yap, C. K. Lai, R. M. De La Rue, H. Ahmad, *Sci. Rep.* 2016, 6, 23813.
 51. X. Zheng, B. Jia, H. Lin, L. Qiu, D. Li, M. Gu, *Nat. Commun.* 2015, 6, 8433.
 52. Y. Tan, R. He, C. Cheng, D. Wang, Y. Chen, F. Chen, *Sci. Rep.* 2014, 4, 7523.
 53. Y. Tan, S. Chen, D. Dai, *Opt. Express* 2017, 25, 4106.
 54. J. Wu, X. Xu, T. Nguyen, S. Chu, B. Little, R. Morandotti, A. Mitchell, D. J. Moss, *J. Sel. Top. Quantum Electron.*, 2018, 24, 1.
 55. L. Razzari, et al., "CMOS-compatible integrated optical hyper-parametric oscillator," *Nature Photonics*, vol. 4, no. 1, pp. 41–45, 2010.
 56. D. J. Moss, R. Morandotti, A. L. Gaeta, et al., "New CMOS-compatible platforms based on silicon nitride and Hydex for nonlinear optics," *Nature Photonics*, vol. 7, no. 8, pp. 597–607, 2013.
 57. M. Ferrera, L. Razzari, D. Duchesne, et al., "Low-power continuous-wave nonlinear optics in doped silica glass integrated waveguide structures," *Nature Photonics*, vol. 2, no. 12, pp. 737–740, 2008.

58. A. Pasquazi, M. Peccianti, Y. Park, B. E. Little, S. T. Chu, R. Morandotti, J. Azaña, and D. J. Moss, "Sub-picosecond phase-sensitive optical pulse characterization on a chip", *Nature Photonics*, vol. 5, no. 10, pp. 618–623 (2011).
59. D. Duchesne, M. Peccianti, M. R. E. Lamont, et al., "Supercontinuum generation in a high index doped silica glass spiral waveguide," *Optics Express*, vol. 18, no. 2, pp. 923–930, 2010.
60. M. Ferrera, et al., "On-chip CMOS-compatible all-optical integrator", *Nature Communications*, vol. 1, Article 29, 2010.
61. A. Pasquazi, et al., "All-optical wavelength conversion in an integrated ring resonator," *Optics Express*, vol. 18, no. 4, pp. 3858–3863, 2010.
62. A. Pasquazi, Y. Park, J. Azana, et al., "Efficient wavelength conversion and net parametric gain via Four Wave Mixing in a high index doped silica waveguide," *Optics Express*, vol. 18, no. 8, pp. 7634–7641, 2010.
63. M. Peccianti, M. Ferrera, L. Razzari, et al., "Subpicosecond optical pulse compression via an integrated nonlinear chirper," *Optics Express*, vol. 18, no. 8, pp. 7625–7633, 2010.
64. D. Duchesne, M. Ferrera, L. Razzari, et al., "Efficient self-phase modulation in low loss, high index doped silica glass integrated waveguides," *Optics Express*, vol. 17, no. 3, pp. 1865–1870, 2009.
65. A. Pasquazi, M. Peccianti, L. Razzari, D. J. Moss, S. Coen, M. Erkintalo, Y. K. Chembo, T. Hansson, S. Wabnitz, P. Del'Haye, X. X. Xue, A. M. Weiner, and R. Morandotti, "Micro-combs: A novel generation of optical sources," *Physics Reports*, vol. 729, pp. 1–81, Jan 27. 2018.
66. M. Peccianti, et al., "Demonstration of an ultrafast nonlinear microcavity modelocked laser", *Nature Communications*, vol. 3, pp. 765, 2012.
67. M. Kues, et al., "Passively modelocked laser with an ultra-narrow spectral width", *Nature Photonics*, vol. 11, no. 3, pp. 159, 2017.
68. A. Pasquazi, L. Caspani, M. Peccianti, et al., "Self-locked optical parametric oscillation in a CMOS compatible microring resonator: a route to robust optical frequency comb generation on a chip," *Optics Express*, vol. 21, no. 11, pp. 13333–13341, 2013.
69. A. Pasquazi, M. Peccianti, B. E. Little, et al., "Stable, dual mode, high repetition rate mode-locked laser based on a microring resonator," *Optics Express*, vol. 20, no. 24, pp. 27355–27362, 2012.
70. C. Reimer, et al., "Integrated frequency comb source of heralded single photons," *Optics Express*, vol. 22, no. 6, pp. 6535–6546, 2014.
71. C. Reimer, et al., "Cross-polarized photon-pair generation and bi-chromatically pumped optical parametric oscillation on a chip", *Nature Communications*, vol. 6, Article 8236, 2015. DOI: 10.1038/ncomms9236
72. L. Caspani, C. Reimer, M. Kues, et al., "Multifrequency sources of quantum correlated photon pairs on-chip: a path toward integrated Quantum Frequency Combs," *Nanophotonics*, vol. 5, no. 2, pp. 351–362, 2016.

73. C. Reimer et al., "Generation of multiphoton entangled quantum states by means of integrated frequency combs," *Science*, vol. 351, no. 6278, pp. 1176–1180, 2016.
74. M. Kues, et al., "On-chip generation of high-dimensional entangled quantum states and their coherent control", *Nature*, vol. 546, no. 7660, pp. 622–626, 2017.
75. P. Roztock, M. Kues, C. Reimer, B. Wetz, S. Sciara, Y. Zhang, A. Cino, B. E. Little, S. T. Chu, D. J. Moss, and R. Morandotti, "Practical system for the generation of pulsed quantum frequency combs," *Optics Express*, vol. 25, no. 16, pp. 18940–18949, 2017.
76. Y. Zhang, et al., "Induced photon correlations through superposition of two four-wave mixing processes in integrated cavities", *Laser and Photonics Reviews*, vol. 14, no. 7, pp. 2000128, 2020. DOI: 10.1002/lpor.202000128
77. M. Kues, C. Reimer, A. Weiner, J. Lukens, W. Munro, D. J. Moss, and R. Morandotti, "Quantum Optical Micro-combs", *Nature Photonics*, vol. 13, no.3, pp. 170–179, 2019.
78. C. Reimer, et al., "High-dimensional one-way quantum processing implemented on d-level cluster states", *Nature Physics*, vol. 15, no.2, pp. 148–153, 2019.
79. B. Corcoran, et al., "Ultra-dense optical data transmission over standard fiber with a single chip source", *Nature Communications*, vol. 11, Article:2568, 2020.
80. X. Xu, et al., "Photonic perceptron based on a Kerr microcomb for scalable high speed optical neural networks", *Laser and Photonics Reviews*, vol. 14, no. 8, 2020. DOI:10.1002/lpor.202000070.
81. X. Xu et al., "11 TOPs photonic convolutional accelerator for optical neural networks", *Nature*, vol. 589, 44–51 (2021).
82. X.Xu et al., "11 TeraFLOPs per second photonic convolutional accelerator for deep learning optical neural networks", arXiv:2011.07393 [cs.NE] (2021).
83. D.J.Moss, "11 Tera-FLOP/s photonic convolutional accelerator and deep learning optical neural networks", *Research Square* (2021). DOI: 10.21203/rs.3.rs-493347/v1
84. T. G. Nguyen et al., "Integrated frequency comb source-based Hilbert transformer for wideband microwave photonic phase analysis," *Opt. Express*, vol. 23, no. 17, pp. 22087–22097, Aug. 2015.
85. X. Xu et al., "Reconfigurable broadband microwave photonic intensity differentiator based on an integrated optical frequency comb source," *APL Photonics*, vol. 2, no. 9, 096104, Sep. 2017.
86. X. Xu, M. Tan, J. Wu, R. Morandotti, A. Mitchell, and D. J. Moss, "Microcomb-based photonic RF signal processing", *IEEE Photonics Technology Letters*, vol. 31 no. 23 1854–1857, 2019.
87. X. Xu, et al., "Advanced RF and microwave functions based on an integrated optical frequency comb source," *Opt. Express*, vol. 26, no. 3, pp. 2569–2583, Feb. 2018.
88. X. Xu, et al., "Broadband RF channelizer based on an integrated optical frequency Kerr comb source," *Journal of Lightwave Technology*, vol. 36, no. 19, pp. 4519–4526, 2018.
89. X. Xu, et al., "Continuously tunable orthogonally polarized RF optical single sideband generator based on micro-ring resonators," *Journal of Optics*, vol. 20, no. 11, pp. 115701. 2018.

90. X. Xu, et al., "Orthogonally polarized RF optical single sideband generation and dual-channel equalization based on an integrated microring resonator," *Journal of Lightwave Technology*, vol. 36, no. 20, pp. 4808–4818. 2018.
91. X. Xu, et al., "Photonic microwave true time delays for phased array antennas using a 49 GHz FSR integrated optical micro-comb source," *Photonics Res*, vol. 6, no. 5, pp. B30-B36, 2018.
92. X. Xu, et al., "Advanced adaptive photonic RF filters with 80 taps based on an integrated optical micro-comb source," *Journal of Lightwave Technology*, vol. 37, no. 4, pp. 1288–1295, 2019.
93. X. Xu, et al., "Broadband microwave frequency conversion based on an integrated optical micro-comb source", *Journal of Lightwave Technology*, vol. 38 no. 2, pp. 332–338, 2020.
94. M. Tan, et al., "Photonic RF and microwave filters based on 49GHz and 200GHz Kerr microcombs", *Optics Comm.* vol. 465, 125563. 2020.
95. X. Xu, et al., "Broadband photonic RF channelizer with 90 channels based on a soliton crystal microcomb", *Journal of Lightwave Technology*, vol. 38, no. 18, 5116–5121, Sept. 15 (2020). doi: 10.1109/JLT.2020.2997699
96. X. Xu, et al., "Photonic RF and microwave integrator with soliton crystal microcombs", *IEEE Transactions on Circuits and Systems II: Express Briefs*, vol. 67, no. 12, pp. 3582–3586, 2020.
97. X. Xu, et al., "Photonic RF phase-encoded signal generation with a microcomb source", *J. Lightwave Technology*, vol. 38 (7) pp. 1722–1727, 2020.
98. X. Xu, et al., "High performance RF filters via bandwidth scaling with Kerr micro-combs," *APL Photonics*, vol. 4, no. 2, pp. 026102. 2019.
99. M. Tan, et al., "Microwave and RF photonic fractional Hilbert transformer based on a 50 GHz Kerr micro-comb", *Journal of Lightwave Technology*, vol. 37, no. 24, pp. 6097–6104, 2019.
100. M. Tan, et al., "RF and microwave fractional differentiator based on photonics", *IEEE Transactions on Circuits and Systems: Express Briefs*, vol. 67, no. 11, pp. 2767–2771, 2020.
101. M. Tan, et al., "Photonic RF arbitrary waveform generator based on a soliton crystal micro-comb source", *Journal of Lightwave Technology*, vol. 38, no. 22, pp. 6221–6226, Oct 22, 2020.
102. H. Bao, et al., "Laser cavity-soliton microcombs," *Nature Photonics*, vol. 13, no. 6, pp. 384–389, Jun. 2019.
103. H. Bao et al., "Turing patterns in a fibre laser with a nested micro-resonator: robust and controllable micro-comb generation", *Physical Review Research*, vol. 2, pp. 023395, 2020.
104. L. D. Lauro, J. Li, D. J. Moss, R. Morandotti, S. T. Chu, M. Peccianti, and A. Pasquazi, "Parametric control of thermal self-pulsation in micro-cavities," *Opt. Lett.* vol. 42, no. 17, pp. 3407–3410, Aug. 2017.
105. H. Bao, et al., "Type-II micro-comb generation in a filter-driven four wave mixing laser," *Photonics Research*, vol. 6, no. 5, pp. B67-B73, 2018.
106. Mengxi Tan, X. Xu, J. Wu, T. G. Nguyen, S. T. Chu, B. E. Little, R. Morandotti, A. Mitchell, and David J. Moss, "Photonic Radio Frequency Channelizers based on Kerr Optical Micro-combs", *Journal of*

- Semiconductors, vol. 42 (4), 041302 (2021). (ISSN 1674–4926). DOI:10.1088/1674-4926/42/4/041302.
107. H.Bao, L.Olivieri, M.Rowley, S.T. Chu, B.E. Little, R.Morandotti, D.J. Moss, J.S.T. Gongora, M.Peccianti and A.Pasquazi, “Laser Cavity Solitons and Turing Patterns in Microresonator Filtered Lasers: properties and perspectives”, Paper No. LA203-5, Paper No. 11672-5, SPIE LASE, SPIE Photonics West, San Francisco CA March 6–11 (2021). DOI:10.1117/12.2576645
 108. Mengxi Tan, X. Xu, J. Wu, A. Boes, T. G. Nguyen, S. T. Chu, B. E. Little, R. Morandotti, A. Mitchell, and David J. Moss, “Advanced microwave signal generation and processing with soliton crystal microcombs”, or “Photonic convolutional accelerator and neural network in the Tera-OPs regime based on Kerr microcombs”, Paper No. 11689-38, PW210-OE201-67, Integrated Optics: Devices, Materials, and Technologies XXV, SPIE Photonics West, San Francisco CA March 6–11 (2021). DOI: 10.1117/12.2584017
 109. Mengxi Tan, Bill Corcoran, Xingyuan Xu, Andrew Boes, Jiayang Wu, Thach Nguyen, Sai T. Chu, Brent E. Little, Roberto Morandotti, Arnan Mitchell, and David J. Moss, “Optical data transmission at 40 Terabits/s with a Kerr soliton crystal microcomb”, Paper No.11713-8, PW210-OE803-23, Next-Generation Optical Communication: Components, Sub-Systems, and Systems X, SPIE Photonics West, San Francisco CA March 6–11 (2021). DOI:10.1117/12.2584014
 110. Mengxi Tan, X. Xu, J. Wu, A. Boes, T. G. Nguyen, S. T. Chu, B. E. Little, R. Morandotti, A. Mitchell, and David J. Moss, “RF and microwave photonic, fractional differentiation, integration, and Hilbert transforms based on Kerr micro-combs”, Paper No. 11713-16, PW210-OE803-24, Next-Generation Optical Communication: Components, Sub-Systems, and Systems X, SPIE Photonics West, San Francisco CA March 6–11 (2021). DOI:10.1117/12.2584018
 111. Mengxi Tan, X. Xu, J. Wu, A. Boes, T. G. Nguyen, S. T. Chu, B. E. Little, R. Morandotti, A. Mitchell, and David J. Moss, “Broadband photonic RF channelizer with 90 channels based on a soliton crystal microcomb”, or “Photonic microwave and RF channelizers based on Kerr micro-combs”, Paper No. 11685-22, PW210-OE106-49, Terahertz, RF, Millimeter, and Submillimeter-Wave Technology and Applications XIV, SPIE Photonics West, San Francisco CA March 6–11 (2021). DOI:10.1117/12.2584015
 112. X. Xu, M. Tan, J. Wu, S. T. Chu, B. E. Little, R. Morandotti, A. Mitchell, B. Corcoran, D. Hicks, and D. J. Moss, “Photonic perceptron based on a Kerr microcomb for scalable high speed optical neural networks”, IEEE Topical Meeting on Microwave Photonics (MPW), pp. 220–224, Matsue, Japan, November 24–26, 2020. Electronic ISBN:978-4-88552-331-1. DOI: 10.23919/MWP48676.2020.9314409
 113. Mengxi Tan, Bill Corcoran, Xingyuan Xu, Andrew Boes, Jiayang Wu, Thach Nguyen, S.T. Chu, B. E. Little, Roberto Morandotti, Arnan Mitchell, and David J. Moss, “Ultra-high bandwidth optical data transmission with a microcomb”, IEEE Topical Meeting on Microwave Photonics (MPW), pp. 78–82. Virtual Conf., Matsue, Japan, November 24–26, 2020. Electronic ISBN:978-4-88552-331-1. DOI: 10.23919/MWP48676.2020.9314476

114. M. Tan, X. Xu, J. Wu, R. Morandotti, A. Mitchell, and D. J. Moss, "RF and microwave high bandwidth signal processing based on Kerr Micro-combs", *Advances in Physics X*, VOL. 6, NO. 1, 1838946 (2020). DOI:10.1080/23746149.2020.1838946.
115. Mengxi Tan, Xingyuan Xu, Jiayang Wu, Thach G. Nguyen, Sai T. Chu, Brent E. Little, Roberto Morandotti, Arnan Mitchell, and David J. Moss, "Photonic Radio Frequency Channelizers based on Kerr Micro-combs and Integrated Micro-ring Resonators", *JOSarXiv.202010.0002*.
116. Mengxi Tan, Xingyuan Xu, David Moss "Tunable Broadband RF Photonic Fractional Hilbert Transformer Based on a Soliton Crystal Microcomb", *Preprints*, DOI: 10.20944/preprints202104.0162.v1
117. Mengxi Tan, X. Xu, J. Wu, T. G. Nguyen, S. T. Chu, B. E. Little, R. Morandotti, A. Mitchell, and David J. Moss, "Orthogonally polarized Photonic Radio Frequency single sideband generation with integrated micro-ring resonators", *Journal of Semiconductors*, vol. 42 (4), 041305 (2021). DOI: 10.1088/1674-4926/42/4/041305.
118. Mengxi Tan, Xingyuan Xu, Jiayang Wu, Bill Corcoran, Andreas Boes, Thach G. Nguyen, Sai T. Chu, Brent E. Little, Roberto Morandotti, Arnan Mitchell, and David J. Moss, "Integral order photonic RF signal processors based on a soliton crystal micro-comb source", to be published, *IOP Journal of Optics* (2021). to arxiv
119. Mengxi Tan, Xingyuan Xu, Jiayang Wu, Bill Corcoran, Andreas Boes, Thach G. Nguyen, Sai T. Chu, Brent E. Little, Roberto Morandotti, Arthur Lowery, Arnan Mitchell, and David J. Moss, "Highly reconfigurable RF photonic fractional Hilbert transformer", *Invited Paper, Journal of Lightwave Technology*, vol. 39, Early Access (2021). DOI:10.1109/JLT.2021.3101816.
120. Mengxi Tan, Xingyuan Xu, Jiayang Wu, Roberto Morandotti, Arnan Mitchell, and David J. Moss, "RF and microwave photonic temporal signal processing with Kerr micro-combs", *Advances in Physics X*, VOL. 6, NO. 1, 1838946 (2021). DOI:10.1080/23746149.2020.1838946. DOI: 10.1038/s41586-020-03063-0
121. Yuning Zhang, Jiayang Wu, Yang Qu, Linnan Jia, Baohua Jia, and David J. Moss, "Design and optimization of four-wave mixing in microring resonators integrated with 2D graphene oxide films", *Journal of Lightwave Technology*, vol. 39, Early Access (2021). DOI:10.1109/JLT.2021.3101292.
122. Hamed Arianfard, Jiayang Wu, Saulius Juodkazis, David J. Moss, "Spectral Shaping Based on Integrated Coupled Sagnac Loop Reflectors Formed by a Self-Coupled Wire Waveguide", *IEEE Photonics Technology Letters*, vol. 33, (13) 680–683 (2021). DOI:10.1109/LPT.2021.3088089.
123. Yuning Zhang, Jiayang Wu, Yang Qu, Linnan Jia, Baohua Jia, and David J. Moss, "Optimizing the Kerr nonlinear optical performance of silicon waveguides integrated with 2D graphene oxide films", *Journal of Lightwave Technology*, vol. 39, Issue: 14, Page(s): 4671–4683 (2021). DOI: 10.1109/JLT.2021.3069733.
124. Hamed Arianfard, Jiayang Wu, Saulius Juodkazis and David J. Moss, "Three Waveguide Coupled Sagnac Loop Reflectors for Advanced Spectral Engineering", *Journal of Lightwave Technology*, vol. 39 (11) 3478–3487 (2021). DOI: 10.1109/JLT.2021.3066256.

125. Yang Qu, Jiayang Wu, Yuning Zhang, Yao Liang, Baohua Jia, and David J. Moss, “Analysis of four-wave mixing in silicon nitride waveguides integrated with 2D layered graphene oxide films”, *Journal of Lightwave Technology*, vol. 39 (9) 2902–2910 (2021). DOI: 10.1109/JLT.2021.3059721.
126. Jiayang Wu, Linnan Jia, Yuning Zhang, Yang Qu, Baohua Jia, and David J. Moss, “Graphene oxide: versatile films for flat optics to nonlinear photonic chips”, *Advanced Materials*, vol. 33, (3) 2006415, pp.1–29 (2021). DOI:10.1002/adma.202006415.
127. Hamed Arianfard, Jiayang Wu, Saulius Juodkazis and David J. Moss, “Advanced Multi-Functional Integrated Photonic Filters based on Coupled Sagnac Loop Reflectors”, *Journal of Lightwave Technology*, vol. 39, Issue: 5, pp.1400–1408 (2021). DOI:10.1109/JLT.2020.3037559.
128. Yang Qu, Jiayang Wu, Yunyi Yang, Yuning Zhang, Yao Liang, Houssein El Dirani, Romain Crochemore, Pierre Demongodin, Corrado Sciancalepore, Christian Grillet, Christelle Monat, Baohua Jia, and David J. Moss, “Enhanced nonlinear four-wave mixing in silicon nitride waveguides integrated with 2D layered graphene oxide films”, *Advanced Optical Materials*, vol. 8, (21) 2001048 (2020). DOI: 10.1002/adom.202001048. arXiv:2006.14944.
129. Yuning Zhang, Yang Qu, Jiayang Wu, Linnan Jia, Yunyi Yang, Xingyuan Xu, Baohua Jia, and David J. Moss, “Enhanced Kerr nonlinearity and nonlinear figure of merit in silicon nanowires integrated with 2D graphene oxide films”, *ACS Applied Materials and Interfaces*, vol. 12, (29) 33094 – 33103 June 29 (2020). DOI:10.1021/acami.0c07852
130. Jiayang Wu, Yunyi Yang, Yang Qu, Xingyuan Xu, Yao Liang, Sai T. Chu, Brent E. Little, Roberto Morandotti, Baohua Jia, and David J. Moss, “Graphene oxide waveguide polarizers and polarization selective micro-ring resonators”, *Laser and Photonics Reviews*, vol. 13, (9) 1900056 (2019). DOI:10.1002/lpor.201900056.
131. Jiayang Wu, Yunyi Yang, Yang Qu, Yuning Zhang, Linnan Jia, Xingyuan Xu, Sai T. Chu, Brent E. Little, Roberto Morandotti, Baohua Jia, and David J. Moss, “Enhanced nonlinear four-wave mixing in microring resonators integrated with layered graphene oxide films”, *Small*, vol. 16, (16) 1906563 April 23 (2020).

Figures

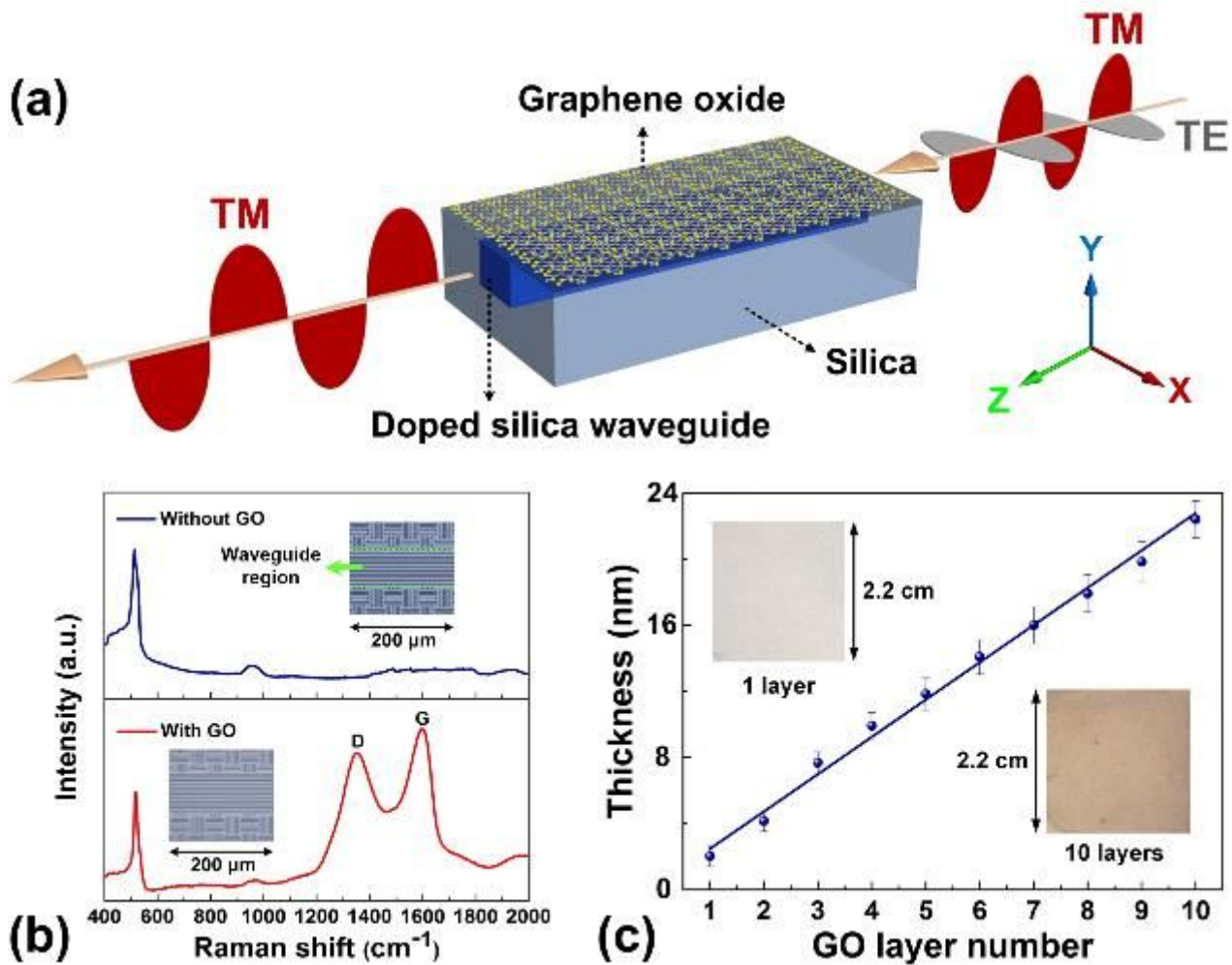


Figure 1

(a) Schematic illustration of GO-coated integrated waveguide polarizer. (b) Raman spectra of the integrated chip without GO and with 2 layers of GO. Insets show the corresponding microscope images with 9 parallel waveguides in the guiding region. (c) Measured GO film thickness versus GO layer number. Insets show the images of a $2.2 \text{ cm} \times 2.2 \text{ cm}$ silica substrate coated with 1 and 10 layers of GO, respectively.

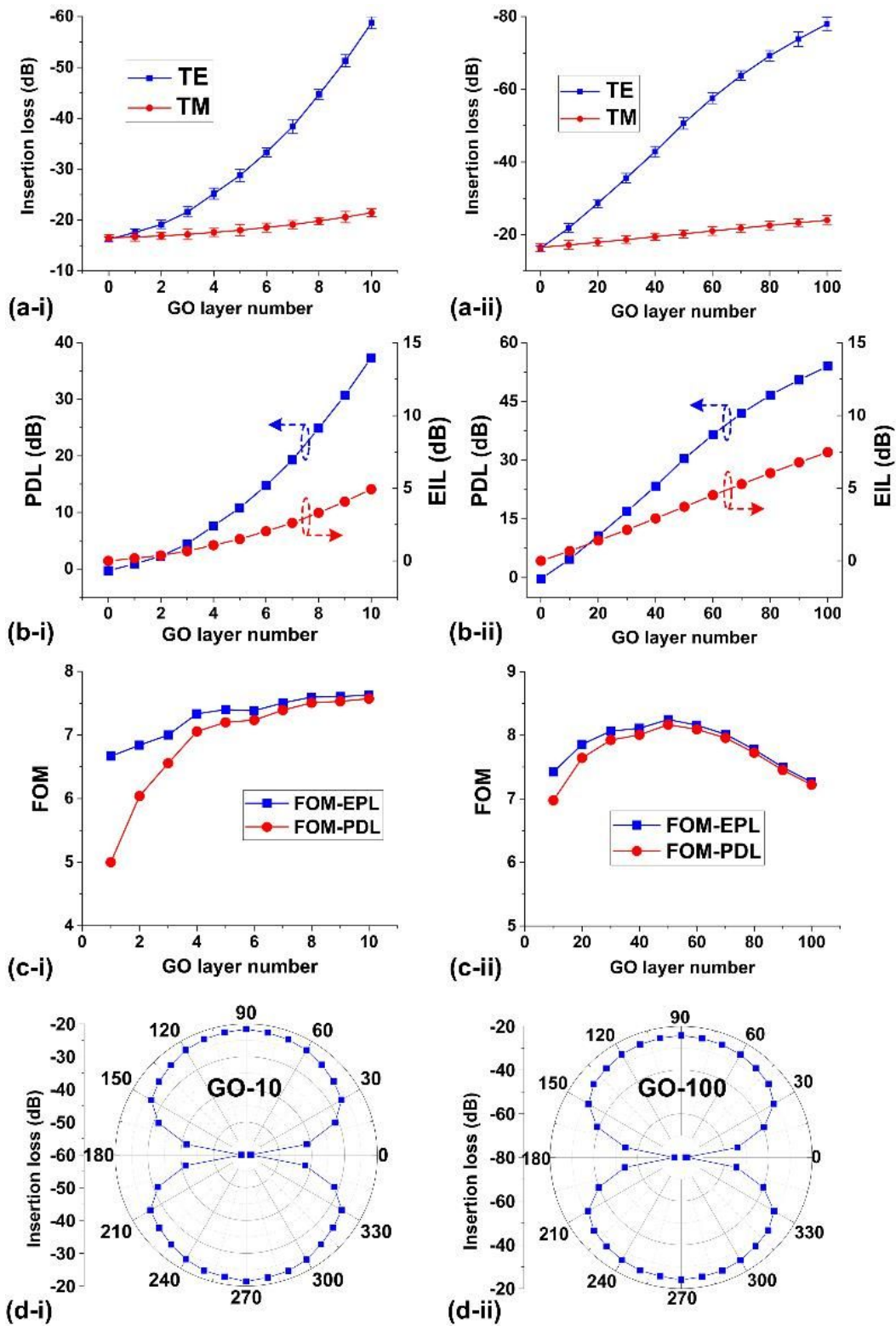


Figure 2

(a) Measured TE and TM polarized insertion loss. (b) Extracted polarization dependent loss (PDL) and excess insertion loss (EIL). (c) Calculated figure of merits (FOMs). In (a) – (c), (i) shows the results for 1.5-cm-long uniformly coated waveguides (0, 1, 2, ..., 10 layers of GO) and (ii) shows the results for 1.5-cm-long waveguides with 2-mm-long patterned GO (0, 10, 20, ..., 100 layers of GO). (d) Polar diagrams presenting the polarizer performance for (i) 1.5-cm GO coating length, 10 layers of GO and (ii) 2-mm GO

coating length, 100 layers of GO. The polar angle represents the angle between the input polarization plane and the substrate. The input CW power and wavelength in (a) and (d) are 0 dBm and 1550 nm, respectively.

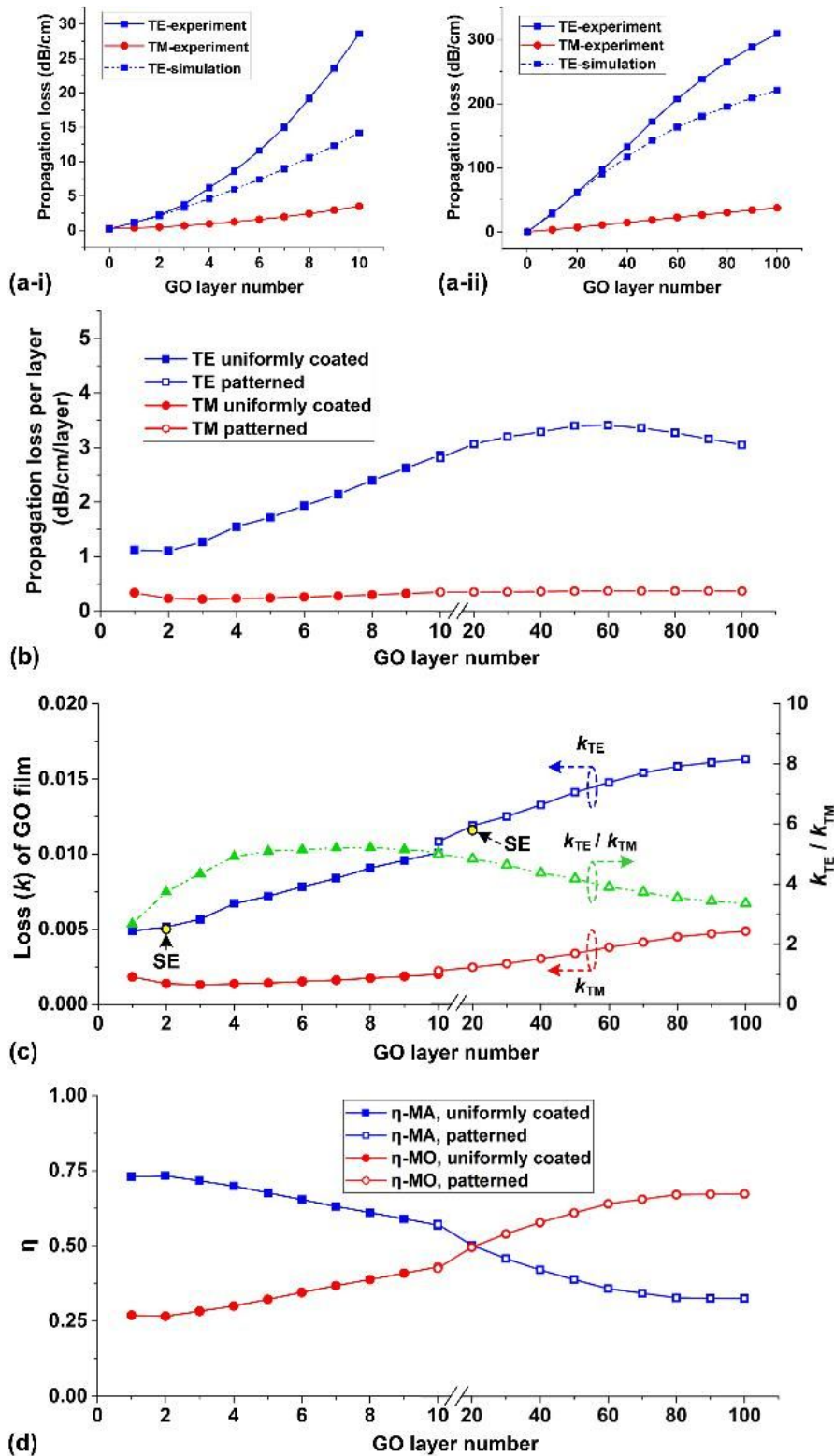


Figure 3

(a) Experimental waveguide propagation loss (extracted from Fig. 2(a)) for (i) a uniformly coated device with 0–10 layers of GO and (ii) a patterned device with 10–100 layers of GO. Simulated TE loss estimated

by using in-plane (TE polarized) n and k for (i) 2 and (ii) 20 layers of GO obtained from ellipsometry measurements in conjunction with mode solving software (assuming constant n , k for different layer numbers in each plot). (b) Experimental loss per layer given by the experimental loss in (a) divided by the number of layers for both polarizations. (c) Material loss of the GO films for TE (k_{TE}) and TM (k_{TM}) polarizations as well as their ratio (k_{TE} / k_{TM}). The two yellow data points (labelled as “SE”) show the in-plane k measured by spectral ellipsometry (SE) for 2 and 20 layers of GO. (d) Fractional contribution to PDL from mode overlap (η_{MO}) and material loss anisotropy (η_{MA}). In (b) – (d), the solid data points refer to the results for a uniformly coated device, whereas the hollow points are for a patterned device.

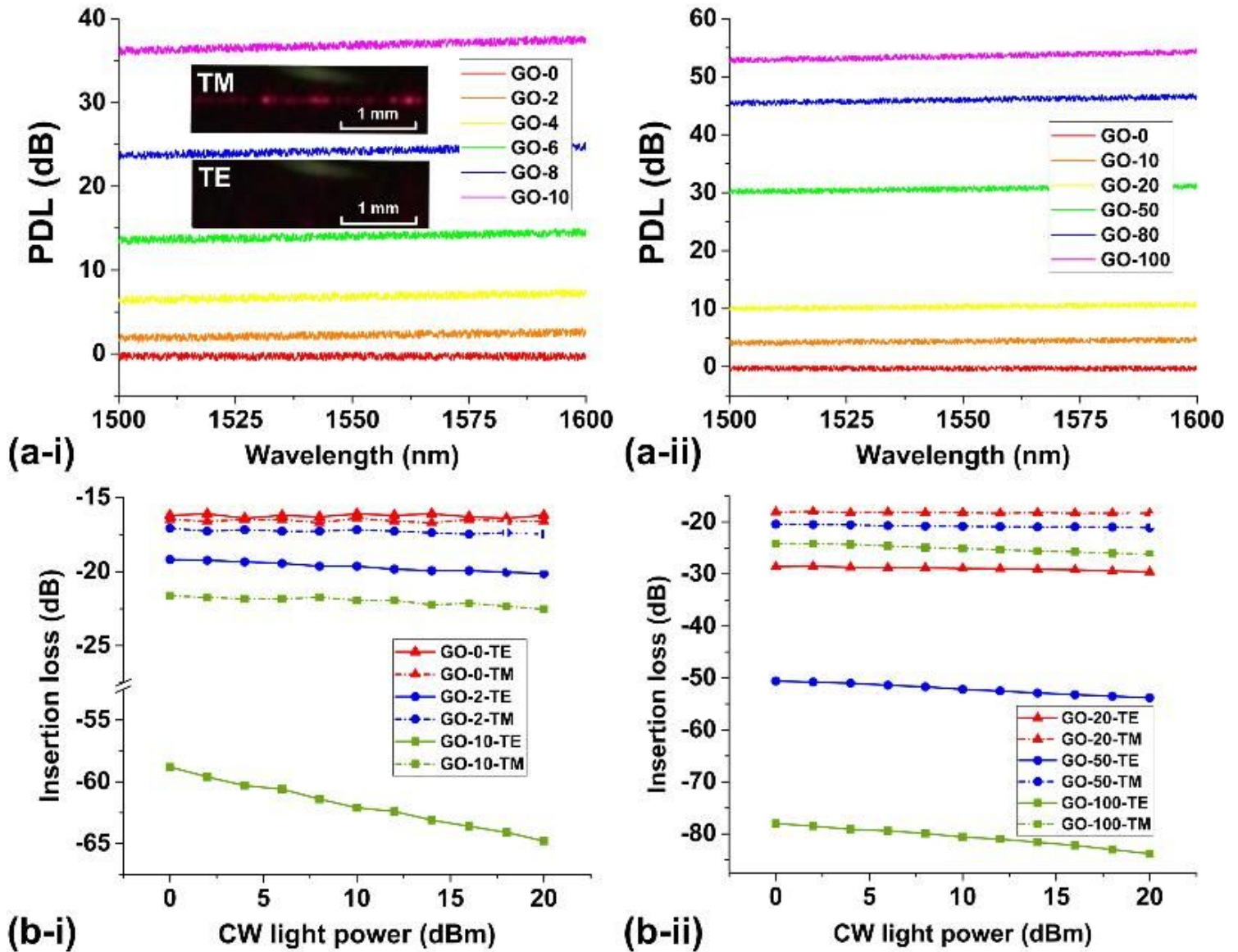


Figure 4

Measured PDL in the wavelength range of 1500 nm ~1600 nm for (i) 1.5-cm GO coating length, 0–10 layers of GO and (ii) 2-mm GO coating length, 0–100 layers of GO. The input CW power is 0 dBm. Insets in (i) show optical images of TM and TE polarized light at a visible wavelength of ~632 nm along the waveguide uniformly coated with 10 layers of GO. (c) Measured TE and TM polarized insertion losses at

different input CW powers for (i) 1.5-cm GO coating length, 0–10 layers of GO and (ii) 2-mm GO coating length, 0–100 layers of GO. The input CW wavelength is 1550 nm.

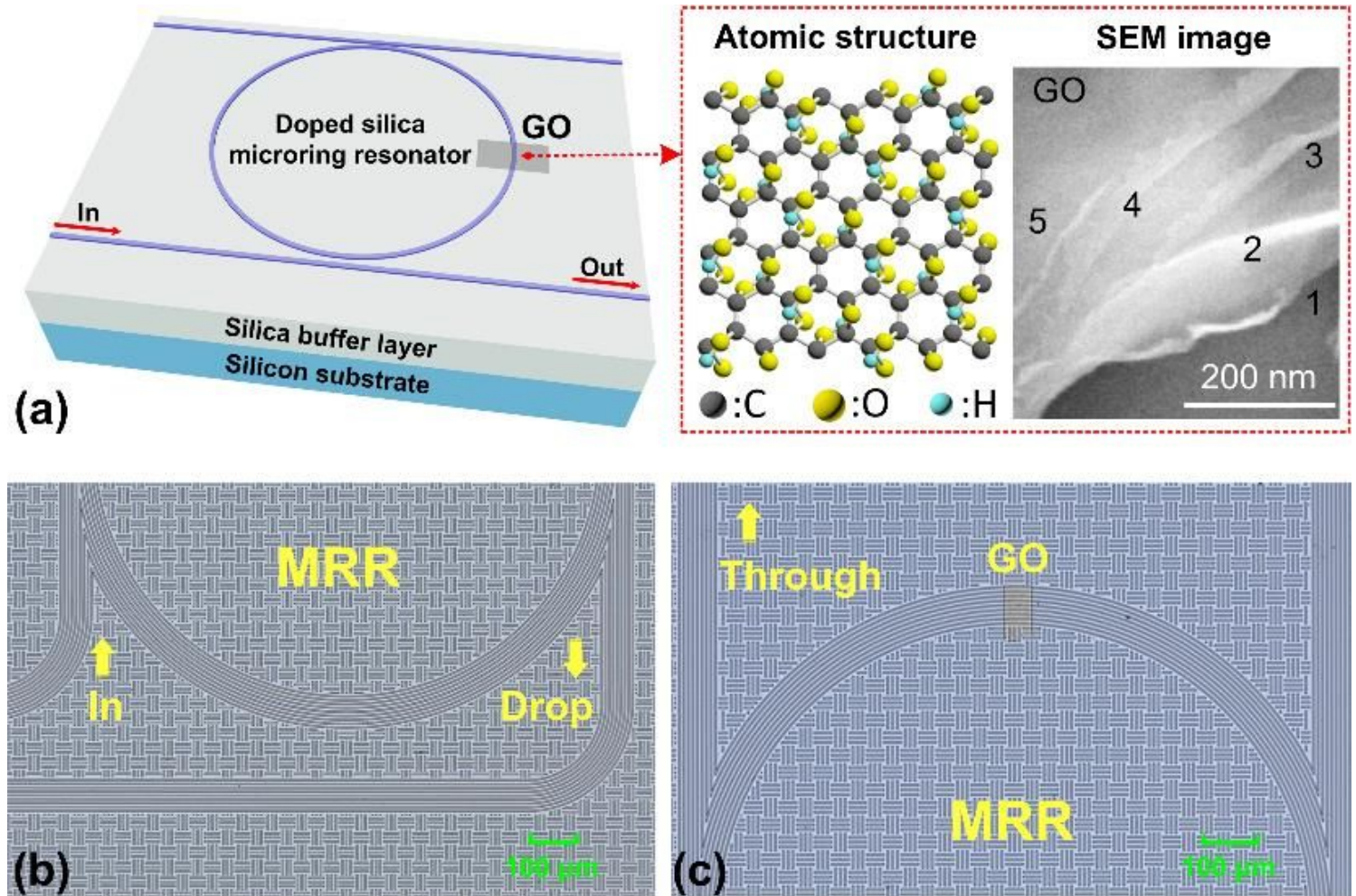


Figure 5

(a) Illustration of GO-based polarization-selective MRR. Insets show schematic atomic structure of GO and a scanning electron microscope (SEM) image of layered GO film. The numbers in the SEM refer to the number of layers for that part of the image. (b)–(c) Microscope images of the integrated MRR uniformly coated with 5 layers of GO and patterned with 50 layers of GO, respectively.

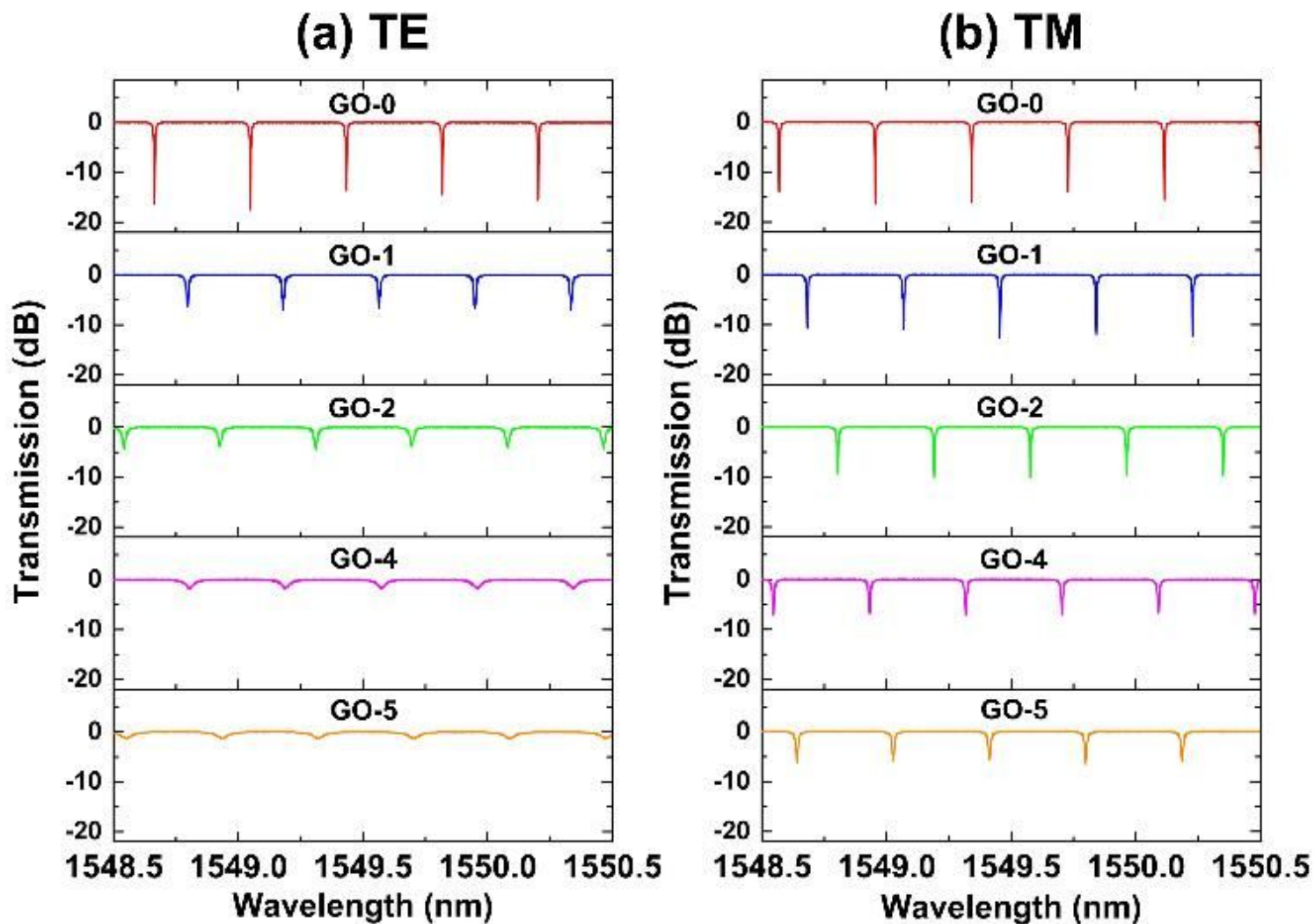


Figure 6

Measured (a) TE and (b) TM polarized transmission spectra of the MRR uniformly coated with 0–5 layers of GO.

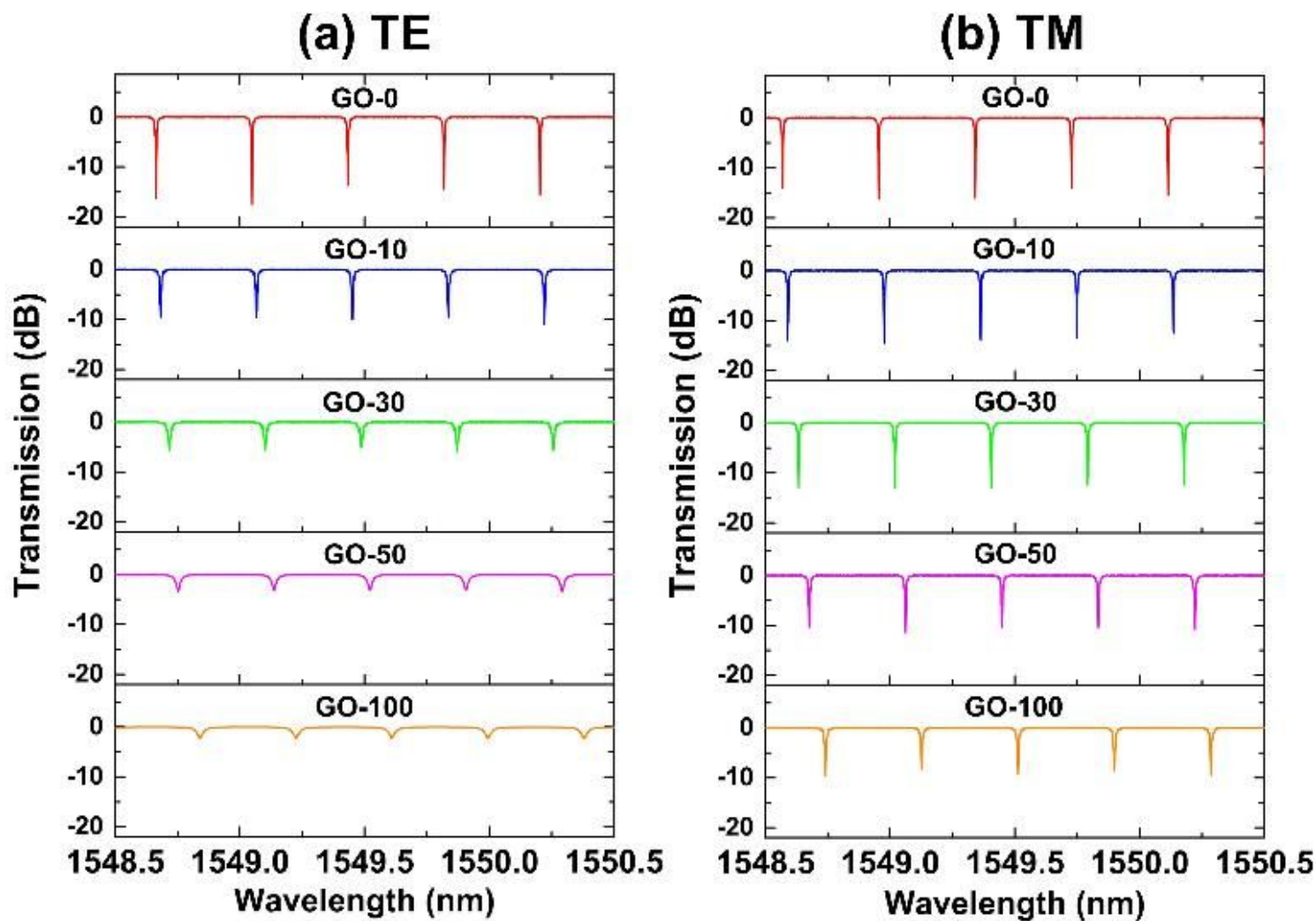


Figure 7

Measured (a) TE and (b) TM polarized transmission spectra of the patterned MRR with 0-100 layers of GO.

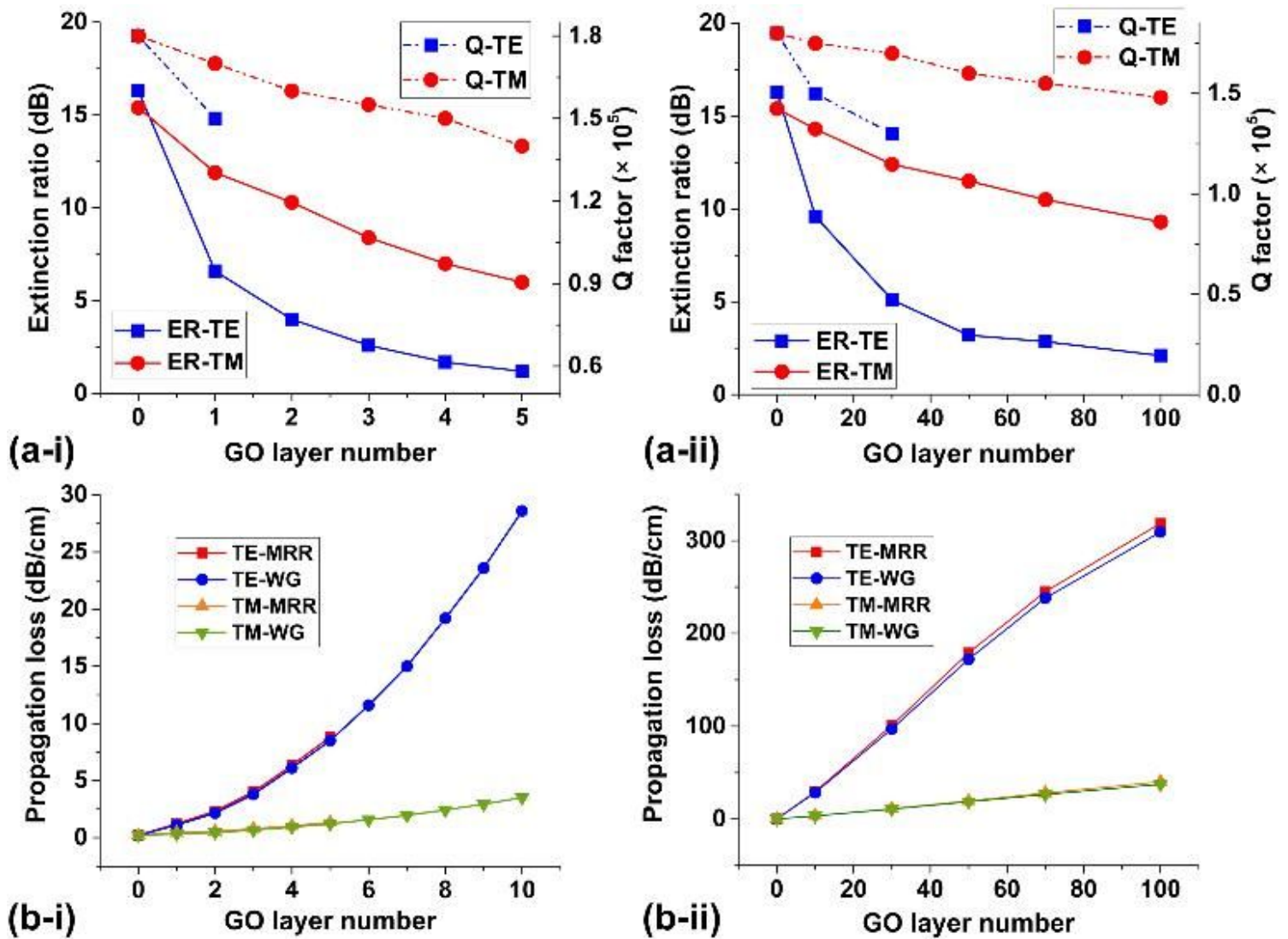


Figure 8

(a) Fit extinction ratios (ERs) and Q factors (Q) for the MRR (i) uniformly coated with 0–5 layers of GO and (ii) patterned with 0–100 layers of GO. The Q factors are not shown when the ER is < 5 dB. (b) Fit propagation loss obtained from the MRR experiment and extracted propagation loss obtained from the waveguide (WG) experiment. (i) 0–10 layers of GO, (ii) 0–100 layers of GO.